


RESEARCH ARTICLE

A hybrid finite element-spectral boundary integral approach: Applications to dynamic rupture modeling in unbounded domains

Xiao Ma¹  | Setare Hajarolasvadi¹ | Gabriele Albertini² | David S. Kammer² | Ahmed E. Elbanna¹

¹Department of Civil and Environmental Engineering, University of Illinois at Urbana-Champaign, Champaign, Illinois, 61801, U.S.A.

²School of Civil and Environmental Engineering, Cornell University, Ithaca, New York, 14853, U.S.A.

Correspondence

Ahmed E. Elbanna, Department of Civil and Environmental Engineering, University of Illinois, Urbana-Champaign, IL 61801, U.S.A.
Email: elbanna2@illinois.edu

Funding information

Basic Energy Sciences, Grant/Award Number: DE-SC0C12504; National Science Foundation, Grant/Award Number: EAR0529922; U.S. Geological Survey, Grant/Award Number: 07HQAG0008

Summary

The finite element method (FEM) and the spectral boundary integral method (SBI) have both been widely used in the study of dynamic rupture simulations along a weak interface. In this paper, we present a hybrid method that combines FEM and SBI through the consistent exchange of displacement and traction boundary conditions, thereby benefiting from the flexibility of FEM in handling problems with nonlinearities or small-scale heterogeneities and from the superior performance and accuracy of SBI. We validate the hybrid method using a benchmark problem from the Southern California Earthquake Center's dynamic rupture simulation validation exercises. We further demonstrate the capability and computational efficiency of the hybrid scheme for resolving off-fault heterogeneities by studying a 2D in-plane shear crack in two different settings: one where the crack is embedded in a high-velocity zone and another where it is embedded in a low-velocity zone. Finally, we discuss the potential of the hybrid method for addressing a wide range of problems in geophysics and engineering.

KEYWORDS

earthquakes, dynamic fracture, finite element, spectral boundary integral

1 | INTRODUCTION

Earthquake ruptures are highly nonlinear and multiscale phenomena. The nonlinearity may arise at different levels. For example, fault friction may depend on the fault slip, slip rate, and deformation history. Thus, the boundary conditions of the fracture problem are nonlinear and the nucleation, propagation, or arrest conditions evolve with time and space and are unknown a priori.¹ Another source of nonlinearity may come from the bulk being loaded beyond its elastic limit, which leads to damage accumulation and inelasticity. In the case of nonplanar faults, the geometric nonlinearity of the fault traces is another contributing factor that may lead to complex patterns of contact and separation. These features usually inhibit the discovery of analytical solutions for this class of problems. Therefore, numerical methods that are capable of treating these nonlinearities are sought to provide insights into the solution behavior. Bulk methods, such as the finite element method (FEM) and finite difference method (FD), as well as boundary integral methods, are among the most widely used approaches for solving these problems.

Abbreviations: FEM, Finite Element Method; LVFZ, Low Velocity Fault Zone; SBI, Spectral Boundary Integral

Aside from the nonlinearity of computational earthquake dynamics, another major challenge is resolving the multiscale nature of the rupture, which exists in both space and time. Spatially, an earthquake may involve several kilometers of fault rupture, whereas the principal slip surfaces, where most of the displacement is accommodated, may be on the order of few millimeters.² Temporally, the time it takes for the stresses to accumulate and initiate an instability is several orders of magnitude larger than the sudden release of energy during an earthquake episode. Hence, a need exists to develop numerical algorithms that resolve these spatial and temporal scales.

Attempts to do such cycle simulations with domain-based methods are rare, partially because discretization of the entire domain is a computational bottleneck.³ On the other hand, boundary integral techniques, which confine the calculations to the fault plane and reduce the dimensions of the problem by one as a result, are more accommodating in this sense. A major contribution in the area was made in the work of Lapusta et al.⁴ Not only did the authors manage to integrate the SBI method into rigorous adaptive time-stepping schemes but they also introduced the concept of mode-dependent time windows, which made it possible to truncate the convolution integrals. These features enable calculations over long durations while capturing the effects of periods with slow tectonic loading marked by episodes of rapid rupture. The main limitation of this method, however, is that it is applicable only to linear-elastic bulks. Furthermore, for problems involving heterogeneities or rough faults, the ability of the method to provide well-defined solutions is compromised, along with the computational efficacy of the method, because it lacks a closed-form representation for the Green's function, which does not allow a straightforward calculation of the spectral transformation of the space convolutions. This makes the computational investigation of problems with rough faults and fault zone complexity extremely expensive.

Unlike SBI methods, domain-based methods are quite flexible in handling material nonlinearities and small-scale heterogeneities⁵⁻⁷ as well as complexities of fault geometry.⁸⁻¹⁰ Lower-order formulations¹¹⁻¹⁶ and high-order formulations¹⁷⁻¹⁹ have been developed over the years. The major limitation of these methods, as discussed previously, stems from the need to discretize the entire domain that may be affected by wave propagation. This, additionally, has led to a wide breadth of research on techniques to truncate the domain without affecting the physical solution, such as boundary viscous damping,²⁰ infinite elements,²¹ and perfectly matching layers.²² However, all these approaches are prone to artificial reflections, and the absorbing boundaries must be taken far enough from the fault plane or the accuracy of the problem will be compromised.

To overcome the limitations of either method and benefit from their strengths, one may envision combining the two into what we have referred to here as the hybrid method. In this hybrid approach, a domain-based numerical method is used to discretize a confined region, namely, a virtual strip, that contains the fault and all near-field nonlinearities or heterogeneities that may potentially affect the rupture dynamics. This strip is then coupled with linear-elastic homogeneous half spaces on each side through a consistent exchange of displacement and traction boundary conditions, whereas the elastodynamic response of these half spaces is captured by SBI.

This idea was first introduced in Hajarolasvadi and Elbanna,²³ where a framework was developed to couple FD and SBI in a consistent manner. This hybrid method was then used to investigate the antiplane propagation of a slip-weakening shear crack in two different settings: (1) a fault with a near-field low-velocity zone and (2) a fault embedded in a homogeneous medium with the possibility of coseismic inelastic strain generation in the vicinity of the fault. In both cases, the method proved to yield results similar to a pure FD scheme, with a smaller computational cost.

In this research, we further extend the hybrid method. Specifically, we formulate the hybrid scheme as a coupling between FEM and SBI in a 2D in-plane setting. This requires a consistent exchange of both the normal and shear components of boundary tractions and displacements. We validate the method by applying it to benchmark problem TPV205-2D from the Southern California Earthquake Center (SCEC). We further demonstrate the capability of the method for handling ruptures in heterogeneous media, first by simulating a 2D in-plane supershear rupture on a crack embedded in a stiff strip and second by simulating a 2D in-plane model with a crack embedded in a low-velocity zone.

The remainder of the paper is organized as follows. In Section 2, we describe the model setup and introduce the numerical scheme. In Section 3, we summarize the results of the simulations for the SCEC benchmark problem, the supershear propagation in heterogeneous media, and the pulse rupture induced by low-velocity fault zone. In Section 4, we discuss the potential of the method as a novel computational earthquake dynamics tool and suggest some future directions. In Section 5, we summarize the conclusions from the hybrid method.

2 | MODEL SETUP AND NUMERICAL SCHEME

We consider a 2D in-plane shear problem in domain Ω , with a prescribed traction boundary S_T and a displacement boundary S_U . The fault is on the boundary S_f .

$$\rho \frac{\partial^2 u_i}{\partial t^2} - \frac{\partial \sigma_{ij}}{\partial x_j} - b_i = 0 \quad \text{in } \Omega, \quad (1)$$

$$\sigma_{ij} n_j = T_i \quad \text{on } S_T, \quad (2)$$

$$u_i = u_i^0 \quad \text{on } S_u, \quad (3)$$

$$R_{ki}(u_i^+ - u_i^-) = \delta_k \quad \text{on } S_f, \quad (4)$$

where u_i is the displacement vector, b_i is the body force vector, Slip is defined by $\delta_i = R_{ij}(u_j^+ - u_j^-)$, where R_{ij} is the rotation matrix that transforms the global coordinates to the local coordinate system of the fault and superscripts + and - indicate the upper and lower fault sides, respectively. If the fault plane is parallel to the x_1 axis, this simplifies to $\delta = u_1^+ - u_1^-$. σ_{ij} is the stress tensor. We assume body forces to be zero and the material behavior to be linear-elastic:

$$\sigma_{ij} = \lambda \delta_{ij} \epsilon_{kk} + 2\mu \epsilon_{ij}, \quad (5)$$

where ϵ_{ij} is the infinitesimal strain tensor and μ, λ the Lamé parameters.

We construct the weak form by computing the dot product of wave Equation 1 and the weighting function ϕ_i and considering the boundary condition Equation 2, we could get the following weak form of the governing equation as follows:

$$-\int_V \sigma_{ij} \phi_{i,j} dV + \int_{S_T} T_i \phi_i dS + \int_{S_{f^+}} T_i^{f^+} \phi_i dS + \int_{S_{f^-}} T_i^{f^-} \phi_i dS - \int_V \rho \ddot{u}_i \phi_i dV = 0. \quad (6)$$

The integral along S_f accounts for the tractions on the fault surfaces. $T_i^{f^+} = \sigma_{ij} n_j^+$ and $T_i^{f^-} = \sigma_{ij} n_j^-$ where n_j^+ and n_j^- are the fault normals for the positive and negative sides of the faults, respectively. The shear component of the fault boundary condition is governed by a friction law. Here, a slip-weakening friction law²⁴ is used. The frictional strength is given by

$$\tau_f(\delta) = \begin{cases} \tau_s - (\tau_s - \tau_r)\delta/\delta_c, & \delta < \delta_c \\ \tau_r, & \delta \geq \delta_c \end{cases} \quad (7)$$

where τ_s and τ_r are the peak and residual frictional strength and δ_c the critical slip required for stress to reach the residual value. Continuity of displacements at the fault is preserved (ie, no slip) if the shear traction is lower than τ_f ; otherwise, local slip occurs.

2.1 | Finite element method

The FEM has been widely used in solving wave propagation problems because of its capability of modeling fault structures with complex geometry and a bulk constitutive response. We limit the description here to the time integration scheme and the reader is referred to standard textbooks^{25,26} for detailed information about the FEM. The step-by-step time integration approach is a central-difference explicit formulation and follows:

$$\dot{u}^{n+1/2} = \dot{u}^{n-1/2} + \Delta t M^{-1}(T^n - f^n), \quad (8)$$

$$u^{n+1} = u^n + \Delta t \dot{u}^{n+1/2}, \quad (9)$$

where $\dot{}$ represents the partial derivative with respect to time and the superscript n indicates the time step index. A lumped mass matrix is used, which eliminates the need to form a global stiffness matrix; therefore, these are all nodal values and the subscript i is omitted. f is the internal force due to the deformation of the solid and Δt the time step. The time stepping of the algorithm must satisfy the stability constraints of the Courant-Friedrichs-Lewy (CFL) condition.²⁵⁻²⁷ The friction law affects the traction boundary condition, hence along the frictional interface Equation 8 becomes

$$\dot{u}^{n+1/2} = \dot{u}^{n-1/2} + \Delta t M^{-1}(T_v^n - f^n). \quad (10)$$

A detailed explanation of the computation of frictional tractions at the interface T_v based on the fault displacement discontinuity is provided in Appendix A using the traction-at-split node (TSN) method.

2.2 | Spectral boundary integral method

The boundary integral method has been used extensively since the mid-1980s to study the propagation of cracks. The main advantage of this method is that it eliminates the need to study wave propagation in the entire domain by using integral relationships between the displacement discontinuities and tractions along the crack path.²⁸ The spectral formulation for this method gives an exact form of such a relationship in the Fourier domain. We use the spectral formulation introduced in Geubelle and Rice,²⁹ where the elastodynamic analysis of each half space is carried out separately. In view of the hybrid method, where SBI constitutes a boundary condition to the FEM model, we focus the description on modeling a half space. The relationship between the traction τ_i and the resulting displacements at the boundary of a half space may be expressed as follows:

$$\begin{aligned}\tau_1^\pm(x_1, t) &= \tau_1^{0\pm}(x_1, t) \mp \frac{\mu}{c_s} \dot{u}_1^\pm(x_1, t) + f_1^\pm(x_1, t) \\ \tau_2^\pm(x_1, t) &= \tau_2^{0\pm}(x_1, t) \mp \frac{(\lambda + 2\mu)}{c_p} \dot{u}_2^\pm(x_1, t) + f_2^\pm(x_1, t),\end{aligned}\quad (11)$$

where \pm represents upper and lower half plane, c_p is the pressure wave speed, c_s is the shear wave speed, τ_i^0 indicates the externally applied load (ie, at infinity), and f_i are linear functionals of the prior deformation history and are computed by the time convolution in the Fourier domain (see Appendix B for more details on the SBI).

The time integration scheme used in the SBI is explicit and given by sampling

$$u_i^{\pm n+1} = u_i^{\pm n} + \Delta t \dot{u}_i^{\pm n+1}, \quad (12)$$

where the velocity is found by solving Equation 11, which results in

$$\begin{aligned}\dot{u}_1^{\pm n+1} &= \pm \frac{c_s}{\mu} \left(f_1^{\pm n+1} + \tau_1^{0\pm} - \tau_1^{\pm n+1} \right) \\ \dot{u}_2^{\pm n+1} &= \pm \frac{c_p}{\lambda + 2\mu} \left(f_2^{\pm n+1} + \tau_2^{0\pm} - \tau_2^{\pm n+1} \right).\end{aligned}\quad (13)$$

2.3 | Hybrid method

The hybrid method is a combination of the FEM and SBI, although any other domain-based method may be used in lieu of FEM. In the hybrid method, all nonlinearities, such as fault surface roughness or material nonlinearity, as well as small-scale heterogeneities, are contained in a virtual strip of a certain width that is introduced for computational purposes only (Figure 1). Appropriate meshing techniques are then used to discretize and model this strip by using FEM. The rest of the domain, which is now homogeneous and linear-elastic, may be modeled as two half spaces coupled with this strip on each side (S^+ , S^-). The elastodynamic response of these half spaces is captured by using the SBI. Through the simulation, the two methods communicate along the virtual boundaries of the strip by exchanging displacement and traction boundary conditions.

The general setup of the hybrid method is shown in Figure 1. The width W_H of the virtual strip depends on the nature of the problem and may be adjusted to contain the heterogeneities, nonlinearities, and other fault zone complexities. A more elaborate explanation for how this adjustment may be accomplished is offered in Section 4.

We apply a staggered coupling approach, in which the FEM and SBI share nodes at the (virtual) infinite boundary. The shared nodes are part of the displacement boundary of the FEM. While FEM provides SBI with the tractions along the virtual boundary, SBI returns the displacement that is to be imposed on S^\pm of FEM. The detailed step-by-step procedure is as follows:

1. Solve full time step within the FEM by solving Equations 8 to 9 (FEM interior nodes only).
2. Set interface tractions in the SBI equal to the internal force from FEM: $\tau_i^{n,\text{SBI}} = f_i^{n,\text{FEM}}$, where f_i^n is given through Equation 8.
3. Solve full time step within SBI by solving Equations 13 and 12.
4. Set displacements of the shared nodes in FEM equal to displacement in SBI: $u_i^{n+1,\text{FEM}} = u_i^{n+1,\text{SBI}}$.
5. Return to Step 1 to advance to the next time step.

Other approaches with a prediction and correction of the imposed displacement have been tested and have not shown any substantial improvements on the result.

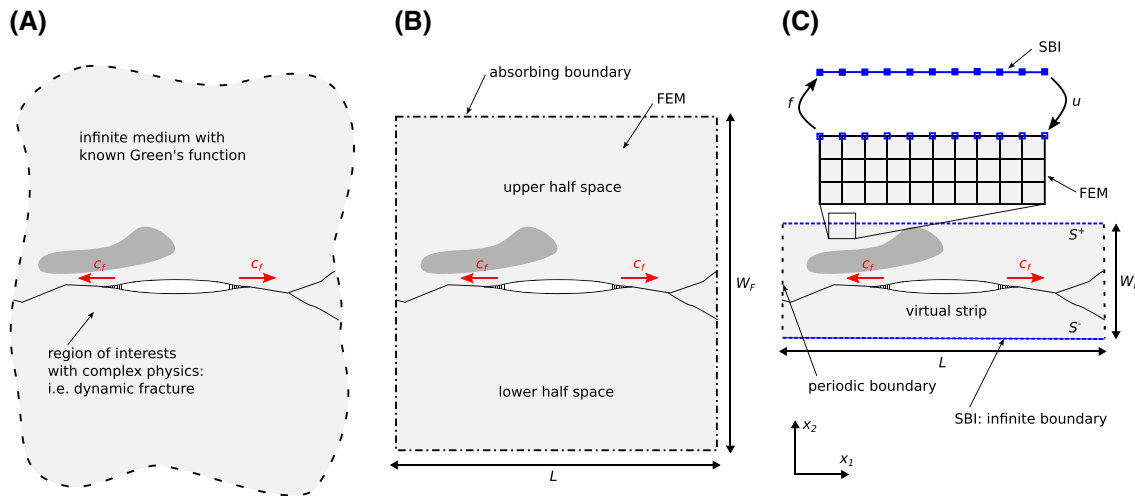


FIGURE 1 Illustration of the hybrid method with coupling of the finite element method (FEM) and spectral boundary integral method (SBI). A, Schematic illustration of problem of interest. Region of interest with complex physics, such as local heterogeneities and crack branching, is embedded in an infinite medium with known Green's function. B, Typical FEM simulation needs a discretized area of size LW_F and absorbing boundaries. The simulated medium is relatively large to avoid interference of numerical reflections at the absorbing boundaries with the relevant physics in the region of interest. C, The hybrid method uses SBI to simulate an infinite boundary, which allows to reduce the zone discretized by FEM to a size of LW_H [Colour figure can be viewed at wileyonlinelibrary.com]

3 | RESULTS

We validate the hybrid method with three problems. In the first one, we use the SCEC Benchmark Validation exercises.³⁰ The problem is a dynamic rupture simulation with heterogeneous initial shear stress on the fault. The second problem is a fault embedded in a heterogeneous medium. The third problem is a fault embedded in a Low-Velocity Zone (LVZ). For the three problems, we compare the simulation results from the hybrid method with those from the FEM.

3.1 | SCEC benchmark validation

We validate the hybrid method with benchmark problem TPV205-2D from the SCEC Dynamic Rupture Validation exercises. The problem is a 2D in-plane fault, governed by the linear slip-weakening friction law, embedded in a linear-elastic homogeneous bulk under plane strain conditions (see Figure 2A). The parameters for the TPV205-2D benchmark are summarized in Table 1. The nucleation of rupture is achieved through a 3-km wide overstressed region located at the center of the fault. The initial shear stress on the fault is shown in Figure 2B, where, in addition to the nucleation patch, there are two other patches of different prestress values from the background uniform initial shear stress. The normal stress is uniform along the entire fault length. On the left and right edges of the fault are two strength barriers with length L_s on each side, which have a high enough static frictional strength to stop the rupture from propagating.

We solve the TPV205-2D benchmark with the hybrid method and compare the results with the FEM benchmark results. Figure 3 shows a comparison of the results from the hybrid approach with those of the FEM. Figure 3A,B shows time history plots of the slip, slip rate, and shear traction at a station at the center of the fault and 4.5 km away from the center, respectively. The results match perfectly. Figure 3C shows the spatial distribution of the slip and slip rate with time intervals of one second, beginning at $t = 1$ s and ending at $t = 5$ s. The hybrid scheme accurately captures the rupture nucleation, propagation, and rest. Figure 4A shows the variation of the L_2 norm of the error between the solution from the hybrid method and solution from FEM on the fault plane with mesh refinement. The results suggest the hybrid method converges to FEM method with mesh refinement. Figure 4B suggests that the absolute error in the slip rate inferred by the two methods at the center of the nucleation zone decreases with mesh refinement. One significant advantage of the hybrid method is its capability of truncating the elastodynamic wave field in the vicinity of the fault plane with no artificial reflections from the virtual boundaries. Specifically for this problem, the full finite element domain is 100 km \times 100 km to ensure that no waves will be reflected from the far-field boundaries. However, in the hybrid scheme, the virtual boundary is chosen at a distance of 0.8 km from the fault plane; thus, we need to discretize a domain of only 100 km \times 1.6 km by FEM. Although the problem under consideration is linear-elastic, it serves the purpose of validating the truncation

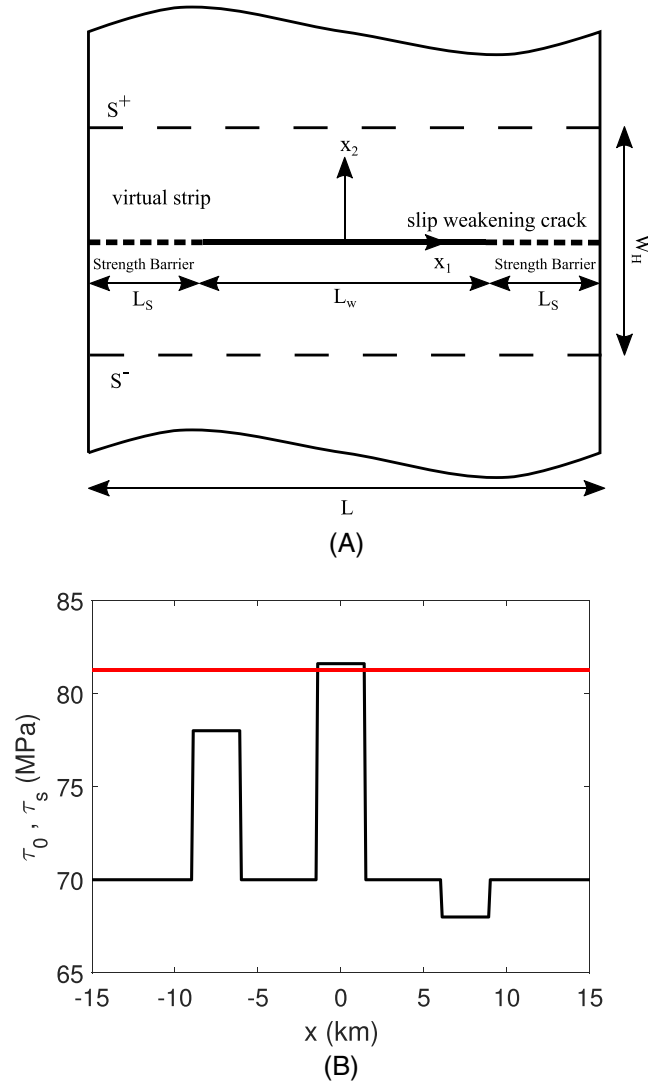


FIGURE 2 A, TPV205-2D problem description. The width of the finite element domain is W_H . The fault length is L , with two strength barriers with high-static friction on the left and right edges of the fault with lengths L_s , respectively. The weakening portion of the fault is L_w . B, Initial shear tractions (in black) on the fault: a strong patch ($\tau_0^w = 68$ MPa), nucleation patch ($\tau_0^{nu} = 81.6$ MPa), and weak patch ($\tau_0^w = 78$ MPa). The static frictional strength is shown in red ($\tau_s = 81.24$ MPa) [Colour figure can be viewed at wileyonlinelibrary.com]

efficiency of the hybrid scheme. When extrapolated to more complex scenarios, this efficient near-field truncation allows the finite element discretization to be limited within a small strip, leading to potential savings in both computational time and memory cost. Here, for the same mesh size $h = 100m$, solving the TPV205-2D problem by using the FEM takes about 1618 seconds. This value reduces to approximately 62 seconds for the hybrid method, suggesting a speedup of 27 times. The other advantage of the hybrid method over FEM is the computational memory savings. For example, at a $100m$ mesh size, FEM takes approximately 191.4 MB of memory, whereas the hybrid method takes only 58.6 MB. The hybrid method uses only 30% of the memory used by the FEM in this case. The savings in computational time and memory cost are expected to become more significant with an increase in problem size and refinement level as we elaborate further in the Discussion section.

3.2 | Supershear rupture transition in a heterogeneous medium

Here, we consider a slip-weakening fault in a heterogeneous medium composed of a central stiff strip and a linear-elastic compliant bulk.^{31,32} The parameters of the problem are summarized in Table 2, and the model geometry is described in Figure 5. The initial shear stress is constant along the fault plane except in a central patch where the fault is overstressed to force abrupt nucleation of the dynamic event. The width of the overstressed patch is L_{nuc} , which is the characteristic

TABLE 1 Problem parameters for the SCEC Benchmark TPV205-2D

Parameter	Symbol	Value
Density (kg/m^3)	ρ	2670.0
Pressure wave speed (km/s)	c_p	6.0
Shear wave speed (km/s)	c_s	3.464
Initial shear stress (nucleation patch) (MPa)	τ_0^{nu}	81.6
Initial shear stress (background) (MPa)	τ_0^{bg}	70.0
Initial shear stress (weak patch) (MPa)	τ_0^w	78.0
Initial shear stress (strong patch) (MPa)	τ_0^s	68.0
Peak frictional strength (MPa)	τ_s	81.24
Residual frictional strength (MPa)	τ_r	63.0
Slip-weakening critical distance (m)	δ_c	0.40
Fault strength barrier length (km)	L_s	35.0
Fault weakening length (km)	L_w	30.0
Distance between two virtual boundaries (km)	W_H	1.6

length scale for frictional instability on linear slip-weakening faults.³³ The normal stress is uniform everywhere. The fault bisects a stiff strip with a total width of $2R$. We choose to locate the virtual boundary at 2.0 km from the fault plane; thus, it is located entirely within the more compliant bulk material.

We compare the slip, slip rate, and shear traction results from the hybrid method and the FEM (Figure 6A) at the center of the fault as well as 4.5 km away from the center (Figure 6B). The hybrid method shows excellent agreement with the benchmark finite element solution. Figure 6C shows snapshots of the slip and slip rate evolution at times 1, 2, 4, 6, and 8 seconds. Because of the reflection from the bimaterial interface, the reflected waves continuously enhance the rupture and eventually enable the transition from subshear to supershear rupture. Subshear rupture occurs when the rupture speed is slower than the shear wave speed while supershear rupture occurs when the rupture speed exceeds that of the shear wave speed but is lower than the pressure wave speed. The hybrid method perfectly captures the complexity of the supershear transition through the Burridge-Andrews mechanism.^{12,34} Figure 7 shows the contour of velocity magnitude distribution at the end of the simulation from FEM and the hybrid method. The hybrid method successfully captures the Mach cone signifying the supershear rupture without any artifacts from the domain truncation. The virtual boundaries are perfectly transparent, resulting in no reflection of the Mach cone rays. Figure 8A shows L_2 norm of the error between the solution from the hybrid method and the solution from FEM on the fault plane with mesh refinement. The results from the hybrid method converge to ones from FEM with mesh refinement. Figure 8B suggests that the absolute error in the slip rate inferred by the two methods at the center of the nucleation zone decreases with mesh refinement. At a 100-m discretization, the simulation time of the hybrid method is approximately 93 seconds, whereas the simulation time of the full FEM is more than 1600 seconds, suggesting the hybrid method is approximately 17 times faster than FEM in this case. Furthermore, in the hybrid scheme, the finite element discretization is limited to a small strip in the vicinity of the fault plane rather than domain-wide discretization. At a 100-m mesh size, the hybrid method uses 77.1 MB of memory, whereas the FEM uses 148 MB. Therefore, the hybrid method uses almost half the memory required by the FEM.

3.3 | Pulse-like ruptures induced by low-velocity fault zones

Low-velocity fault zones (LVFZs) are found in most mature faults. The width of the LVFZ is about several hundred meters. These zones cause wave velocity reductions ranging from 20% to 60% relative^{32,35-37} to the host rock. If the contrast is strong enough, the rupture in the LVFZ can behave as pulses.

In this section, we consider a slip-weakening fault embedded in a LVFZ, with a wave velocity reduction of 20% with respect to the surrounding country rock. The material properties are summarized in Table 3. The model geometry is described in Figure 5 but with inverted material properties. The initial shear stress is constant along the fault plane except in a central patch where the fault is overstressed to force abrupt nucleation of the dynamic event. The width of the overstressed patch is 1.6 km. The normal stress is uniform everywhere. The fault plane bisects the LVFZ which has a total width of 1.6 km. We choose to locate the virtual boundary at 1.2 km from the fault plane.

We compare the slip, slip rate, and shear traction results from the hybrid method and FEM methods Figure 9A at the center of the fault as well as 4.5 km away from the center Figure 9B. The hybrid method shows excellent agreement with

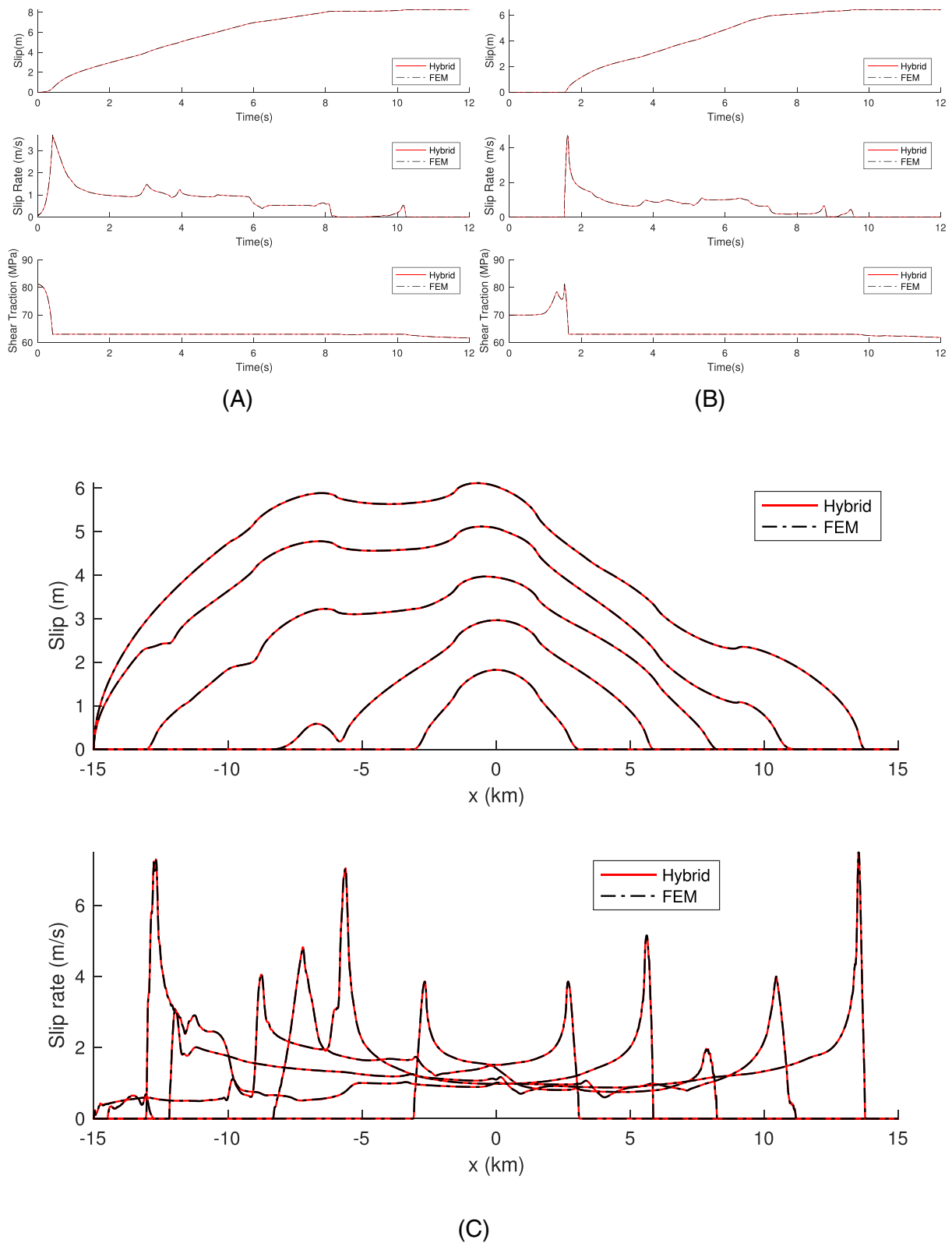
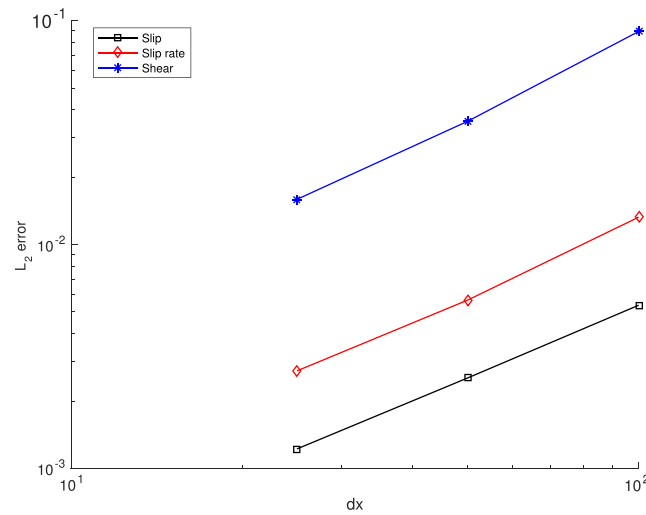
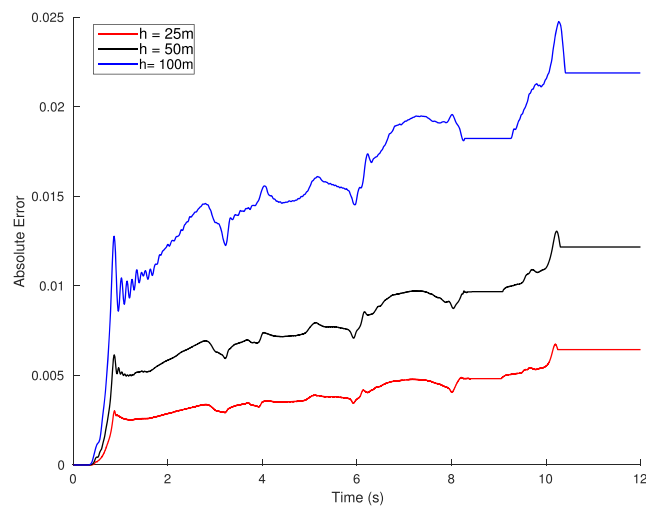


FIGURE 3 TPV205-2D simulation comparing the hybrid method (in red) with the finite element method (FEM; in black) when using a mesh size of $h = 25m$: A, Time history of the slip, slip rate, and shear traction at the station in the center of the fault. B, Time history of the slip, slip rate, and shear traction at a station 4.5 km away from the center of the fault. C, Snapshots of the slip and slip rate at $t = 1$ s, $t = 2$ s, $t = 3$ s, $t = 4$ s, and $t = 5$ s. The results from the hybrid method match those of the finite element benchmark solution perfectly in the nucleation, propagation, and reset of the rupture. The colored figure is available in the electronic version only [Colour figure can be viewed at wileyonlinelibrary.com]



(A)



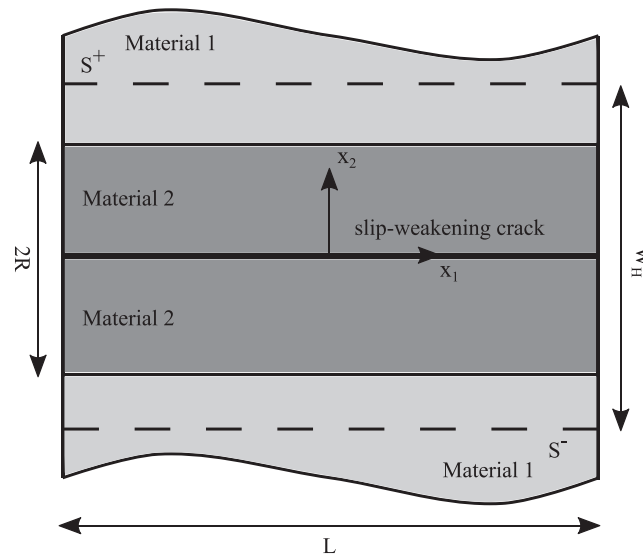
(B)

FIGURE 4 A, L_2 error for the slip, slip rate, and shear traction versus mesh size. With mesh refinement, the hybrid method converges to the FEM solution. B, Absolute error of the slip rate measured at the center of the fault and its evolution with respect to time for different mesh sizes, $h = 25m$, $h = 50m$, and $h = 100m$. The error is reduced with mesh refinement. The color figure is available in the electronic version only [Colour figure can be viewed at wileyonlinelibrary.com]

the benchmark finite element solution. Figure 9C shows snapshots of the slip and slip rate evolution at times 1, 2, 4, 6, 8, and 10 seconds. Since the reflection wave from the boundary of the LVFZ is an inversion of the incident wave for a certain range of incidence angles,³⁵ under certain circumstances, the reflected wave could unload the fault, generating a slip pulse. The slip pulse is observed in Figure 9C. After the nucleation of the rupture, due to the reflection from the boundary of the LVFZ, the crack-like rupture splits into a pulse-like rupture and a crack-like rupture. Figure 10A shows L_2 norm of the error between the solution from the hybrid method and solution from FEM on the fault plane with mesh refinement. The results suggest the hybrid method converges to the FEM method with mesh refinement. Figure 10B suggests that the absolute error in the slip rate inferred by the two methods at the center of the nucleation zone decreases with mesh refinement. The efficient near-field truncation allows the finite element discretization to be limited within a small strip, leading to potential savings in both computational time and memory cost. For the same mesh size $h = 100m$, solving the LVFZ problem by using FEM takes 2288 seconds. This value reduces to 104 seconds for the hybrid method, corresponding to a speedup of 22 times. The saving in memory is significant. For mesh size $h = 100m$, the hybrid method uses approximately 62.7 MB, whereas FEM uses nearly 238 MB. The hybrid method only uses about 26% of the memory that FEM uses.

TABLE 2 Problem parameters for fault-embedded heterogeneous medium

Parameter	Symbol	Value
Density (kg/m^3)	ρ	2670.0
Pressure wave speed (material 1) (km/s)	c_p^{Mat1}	4.8
Shear wave speed (material 1) (km/s)	c_s^{Mat1}	2.771
Pressure wave speed (material 2) (km/s)	c_p^{Mat2}	6.0
Shear wave speed (material 2) (km/s)	c_s^{Mat2}	3.464
Initial shear stress (nucleation patch) (MPa)	τ_0^{nu}	31.0
Initial shear stress (background) (MPa)	τ_0^{bg}	27.5
Peak frictional strength (MPa)	τ_s	30.0
Residual frictional strength (MPa)	τ_r	25.0
Slip-weakening critical distance (m)	δ_c	0.20
Fault length (km)	L	100
Distance between two virtual boundaries (km)	W_H	4.0

**FIGURE 5** Problem geometry description for a fault embedded in a heterogeneous medium. The fault is embedded in a layer with stiffer material properties (material 2), and the surrounding bulk material is material 1. The extension of material 2 from the fault surface is R in each half plane. The virtual boundary is located at $W_H/2$ from the fault surface on each half plane. The length of the fault is L

4 | DISCUSSION

In the previous section, we validated the hybrid method with a SCEC benchmark problem and further showed its flexibility and performance superiority for problems involving near-field heterogeneities. The method proposed takes its adaptability in handling nonlinearities or heterogeneities from FEM and its computational efficiency from SBI. Furthermore, it owes its excellent performance to the accuracy of the boundary conditions, which eliminate any artificial reflections and make it possible to have the virtual boundaries arbitrarily close to the fault plane as long as the remainder of the domain is linear-elastic and homogeneous. The resulting savings in computational resources may then be redirected to study fault-zone nonlinearities with a higher resolution or large-scale nonlinear problems. We believe this may be the first stepping-stone to realizing long-duration simulations of full earthquake cycles in a bulk that might have material heterogeneity, material nonlinearity, fault geometry complexity, or a combination thereof.

A direct advantage of limiting the spatial discretization to a small area near the fault zone is that the computational cost for solving the discretized bulk is significantly reduced, which may allow small-scale heterogeneities, such as fault branches and shear bands, as well as complex physics within the fault zone, including spontaneous strain localization³⁸ or small-scale branches, to be incorporated directly into the model.

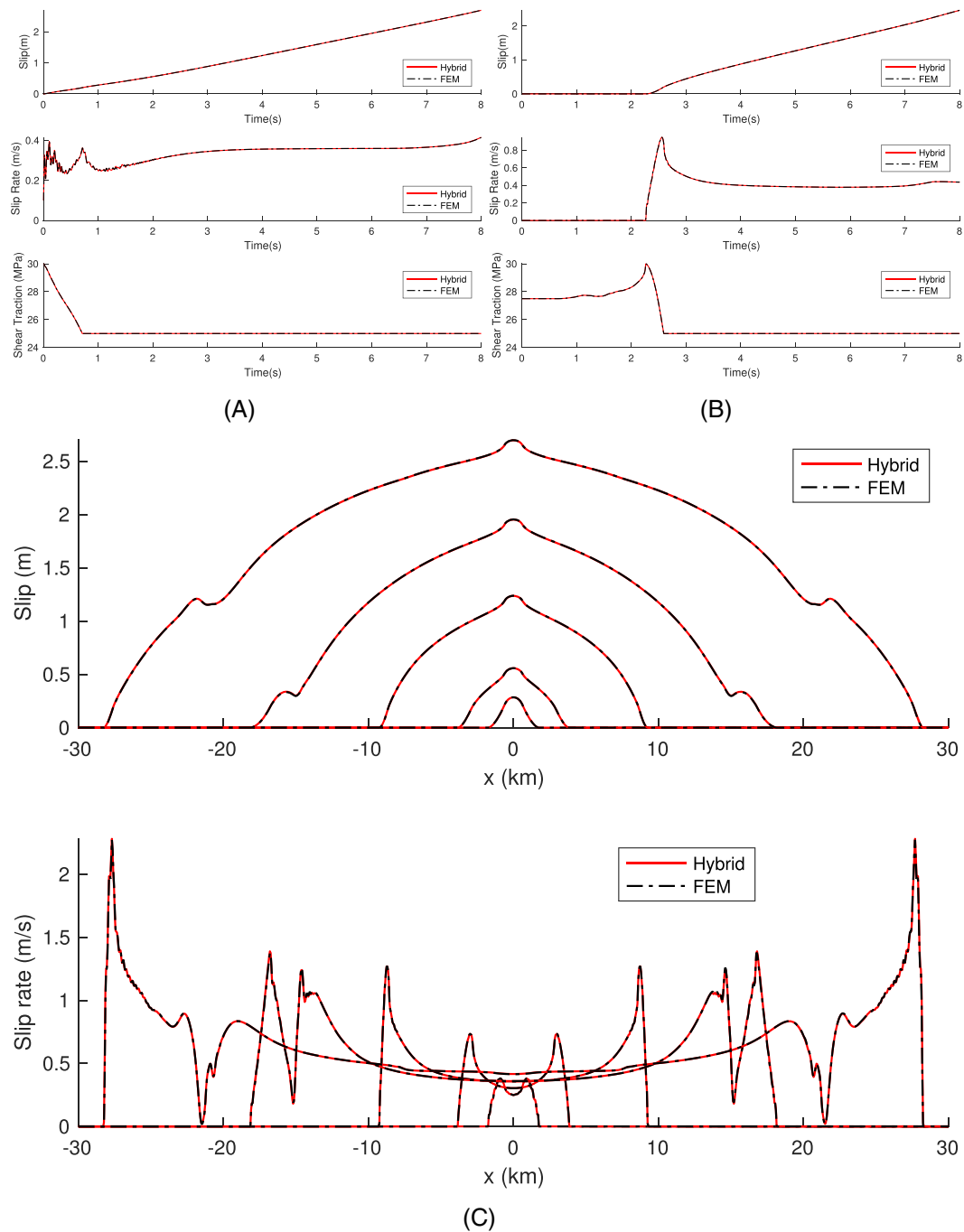


FIGURE 6 Simulation results for a fault embedded in a heterogeneous medium comparing the hybrid method (in red) and the finite element method (FEM; in black) when using a mesh size of $h = 25m$: A, Time history of the slip, slip rate, and shear traction at the station in the center of the fault. B, Time history of the slip, slip rate, and shear traction at the station 4.5 km away from the center of the fault. C, Snapshots of the slip and slip rate at $t = 1s, t = 2s, t = 4s, t = 6s$, and $t = 8s$. The results from the hybrid method match those from the finite element benchmark solution perfectly in the nucleation, propagation, and reset of the rupture. The color figure is available in the electronic version only [Colour figure can be viewed at wileyonlinelibrary.com]

The spectral boundary integral equation provides an accurate boundary condition irrespective of the wave angle incidence. Therefore, unlike other absorbing boundary conditions, such as infinite elements²¹ or even perfectly matching layers,²² where the boundaries must be taken far away from the fault zone to avoid the interference of wave reflections with the physical solution, no artificial reflections are observed in the results obtained from the hybrid method. This result implies that the method may be used as an exact near-field wave truncation algorithm. The consistent exchange of the displacement and traction boundary conditions in this method exploits the same concept as the Dirichlet-to-Neumann

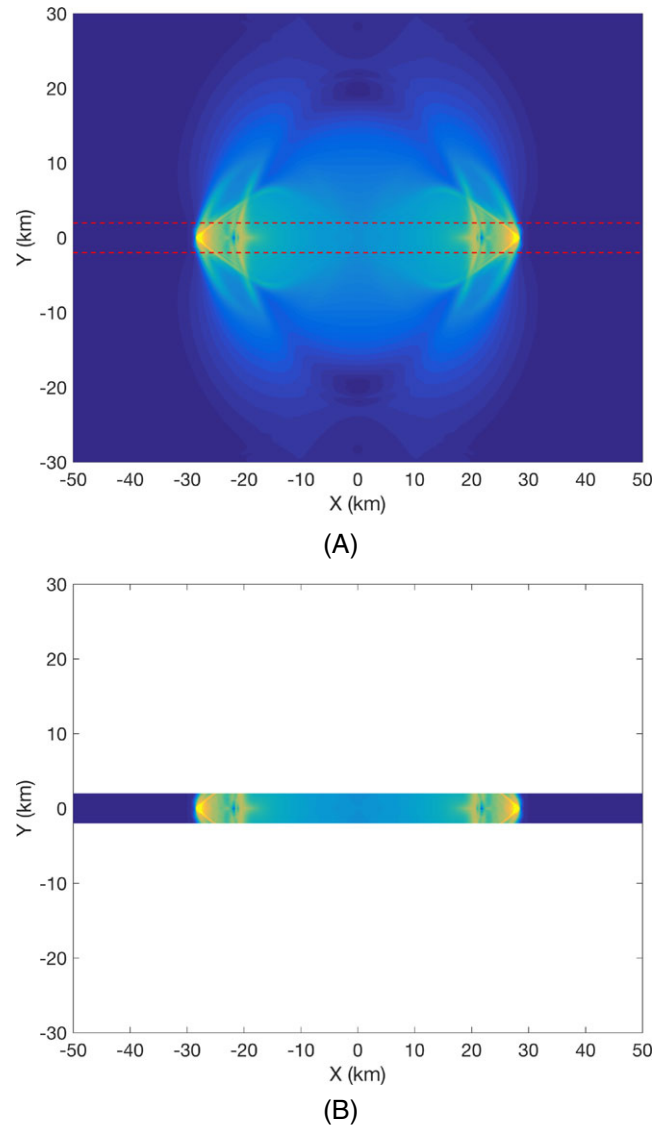


FIGURE 7 Contour of the velocity magnitude in the field: A, Finite element method (FEM) results. B, Hybrid method results. The red dashed line indicates the virtual boundaries located in the hybrid method. The hybrid method captured the truncated Mach cone caused by the supershear rupture. The width of the finite element domain in the hybrid simulation is only 2.4 km, whereas in the FEM simulation, it is 60 km to avoid wave reflection back from the top and bottom boundaries. The hybrid method significantly reduces the computation time and computational memory costs. The color figure is available in the electronic version only [Colour figure can be viewed at wileyonlinelibrary.com]

maps,³⁹ with the difference that the planar virtual boundaries in the hybrid method make it possible to benefit from solving the real space nonlocal boundary condition as a local boundary condition in the Fourier domain, reducing computational costs and enabling efficient parallelization.

Another advantage of this method over previous forms of coupling between bulk and boundary integral methods is that it transforms the nonlocal boundary conditions in space to local ones in the Fourier domain, thereby reducing the cost from N^2 to $N \log N$.⁴ The previous approaches to finite element and boundary integral coupling discretize the spatial convolutions involved in the boundary integral in the real domain, which leads to densely populated stiffness matrices.⁴⁰

The savings in computational time and memory shown in the results is significant. If the fault is discretized by N nodes, the number of computational operations will be $O(N^2 W_F/L)$ when a pure FEM scheme is used. Using the SBI method reduces this number to $O(N \log(N))$.⁴ For the hybrid method, we need $N^2 W_H/L$ FEM nodes to discretize the strip between the virtual boundaries. Thus, the number of computational operations for the hybrid method is $O(N^2 W_H/L + N \log(N))$. The ratio of computational cost for the hybrid method versus the FEM, therefore, is $O(W_H/W_F + L \log(N)/N/W_F)$. For example, for the TPV205-2d SCEC validation problem we have shown, the virtual strip has a width of $W_H = 1.6$ km and

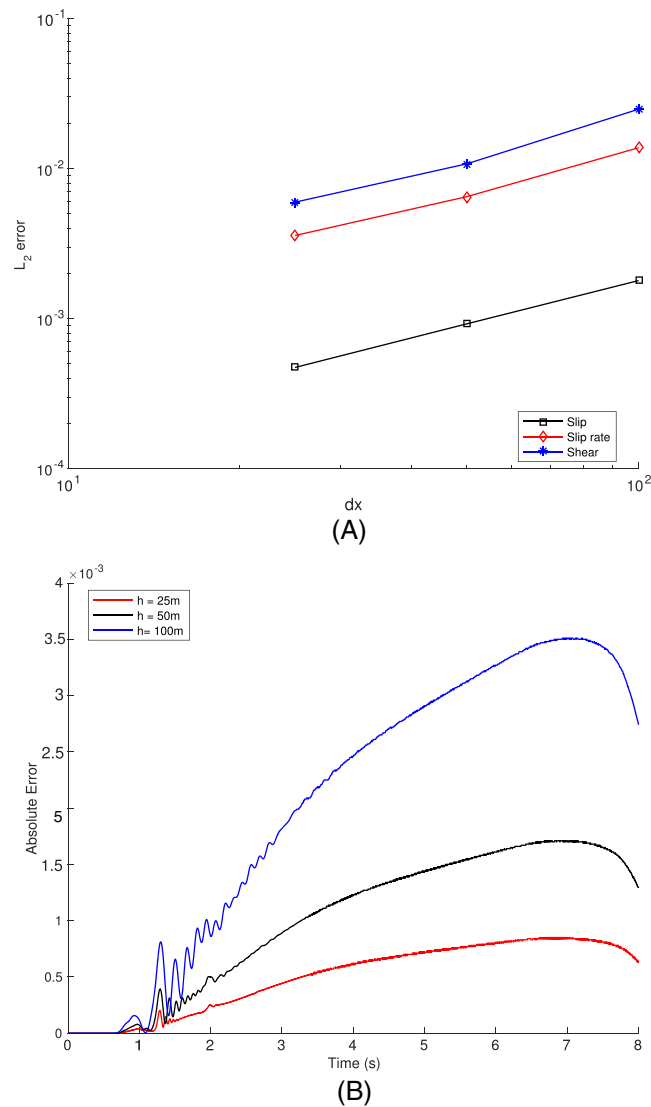


FIGURE 8 A, Heterogeneous medium L_2 error for the slip, slip rate, and shear traction versus mesh size. With mesh refinement, the hybrid method converges to the FEM solution. B, The absolute error of the slip rate measured at the center of the fault and its evolution with respect to time for different mesh sizes, $h = 25m$, $h = 50m$, and $h = 100m$. The error is reduced with mesh refinement. The color figure is available in the electronic version only [Colour figure can be viewed at wileyonlinelibrary.com]

a length of $L = 100$ km and at a mesh size $h = 100m$, the number of discretization points along the fault is $N = 1000$. Therefore, the aforementioned efficiency ratio $W_H/W_F + L \log(N)/N/W_F$ is 0.0229. Based on the numerical simulations, we get an efficiency ratio of 0.0383, which is close to the estimated value.

The characteristics of the method discussed above suggest that it may also potentially be used for long-duration earthquake cycle simulations on faults with near-field material heterogeneities, material nonlinearities, or fault surface complexities. Apart from the computational efficiency of the method, the SBI formulation offers an accurate means for truncating the wave field in both dynamic and quasi-dynamic limits, making the hybrid method capable of capturing the effects of both seismic and interseismic phases of the cycle. Moreover, by exploiting the mode truncation and adaptive time-stepping techniques already embedded in the spectral formulation by Lapusta et al.,⁴ it is possible to resolve the temporal multiscale nature of the rupture in an efficient manner. One can then envision coupling the SBI method with an implicit FEM scheme during the interseismic period to enable this extension.

In Hajarolasvadi and Elbanna,²³ the hybrid method was first introduced for coupling bulk and boundary methods in a 2D antiplane setting. In this study, we have extended the method to 2D in-plane problems. In this case, it is required to couple both the normal and shear components of traction and displacement at the virtual boundaries. Furthermore, because of the existence of fast P -waves and slower S -waves, the time step for integration is limited by the faster P -wave

TABLE 3 Problem parameters for fault embedded in low-velocity zone

Parameter	Symbol	Value
Density (kg/m^3)	ρ	2670.0
Pressure wave speed (material 1) (km/s)	c_p^{Mat1}	6.0
Shear wave speed (material 1) (km/s)	c_s^{Mat1}	3.464
Pressure wave speed (material 2) (km/s)	c_p^{Mat2}	4.8
Shear wave speed (material 2) (km/s)	c_s^{Mat2}	2.771
Initial shear stress (nucleation patch) (MPa)	τ_0^{nu}	31.0
Initial shear stress (background) (MPa)	τ_0^{bg}	26.67
Peak frictional strength (MPa)	τ_s	30.0
Residual frictional strength (MPa)	τ_r	25.0
Slip-weakening critical distance (m)	δ_c	0.20
Fault length (km)	L	100
Distance between two virtual boundaries (km)	W_H	4.8

speed. This situation is slightly more complex than coupling in the antiplane shear setting, where only one wave speed and one component of displacement exist. Nonetheless, the results presented in this paper demonstrate the superior performance of the hybrid method in the 2D in-plane setting and the ability to consistently couple multiple traction and displacement components. With the infrastructure for coupling now available for both in-plane and antiplane settings, the extension to 3D is straightforward because the kernels in the boundary integral convolution are readily available. In future work, we will consider different extensions of the algorithm, such as including the effect of free surfaces in the boundary integral formulation by using the method of images, coupling 3D FEM with SBI, and representation of more realistic friction laws, such as rate and state friction^{41,42} and shear transformation zone models.⁴³⁻⁴⁵

Regarding modeling the lateral boundaries at this point, because the length of the fault under consideration is usually much larger than the lateral dimension in which the nonlinear processes or heterogeneities exist, the waves arriving at the lateral boundaries have almost 90° incidence angles. Under such circumstances, many of the absorbing boundary conditions, including perfectly matching layers and boundary viscous damping, may be used and will exhibit excellent performance because of the near normal incidence. A possible alternative scenario would be using periodic boundary conditions in the FEM domain that are consistent with the periodic boundary conditions for the boundary integral method. For the problems presented here, the results were found to be insensitive to the choice of lateral boundaries. This is partly due to the existence of unbreakable regions near the fault ends that force the rupture to arrest before reaching the lateral boundaries, or due to the domain length being large enough so that waves did not reach the lateral boundaries.

Even though the hybrid method opens the door to exploring a variety of different problems by offering a more flexible and efficient approach, the applicability of this method has limitations. For example, if heterogeneity or inelasticity exists in the far field, the application of the boundary integral equation would no longer be exact. However, in most cases, it is reasonable to assume that such far-field characteristics of the domain do not have a direct impact on the physical solution because the dynamics of rupture are mostly influenced by the local nonlinearities and heterogeneities. The effects of heterogeneities also depend on their distance from the fault zone and the contrast in their properties from that of the bulk. In ground motion applications, the wave amplitude and phase at a location depend on the wave path. Therefore, in this case, it is reasonable for the hybrid method to be used only as a simulator to predict the source characteristics, such as the fault plane slip and slip rate distribution. These data can then be used as inputs to a wave simulation code to track the propagation in globally heterogeneous and inelastic media and to predict ground motion.

Another restriction of the method is that for dynamic heterogeneities, such as off-fault plasticity, we usually do not know the region over which the nonlinearities will act a priori. In the case of off-fault plasticity, we can use previous work in the field,^{7,46-48} which implies that inelasticity and damage will be contained in a narrow region near the fault plane. Hajarolasvadi and Elbanna²³ demonstrated the success of the hybrid scheme in modeling antiplane shear cracks with spontaneous off-fault plastic strain generation by preestimating the size of the plastic region and ensuring that the virtual strip completely enclosed the inelasticity. However, in general, an adaptive scheme can also be used. For example, if the inelastic region grows close to the virtual boundaries, we may move the virtual boundaries away from the fault plane and advance the solution on this modified geometry for the next time steps. The solution on the part added to the virtual strip would then need to be accounted for. This can be done directly by using the history of the solution on the previous virtual boundary and applying the representation theorem.

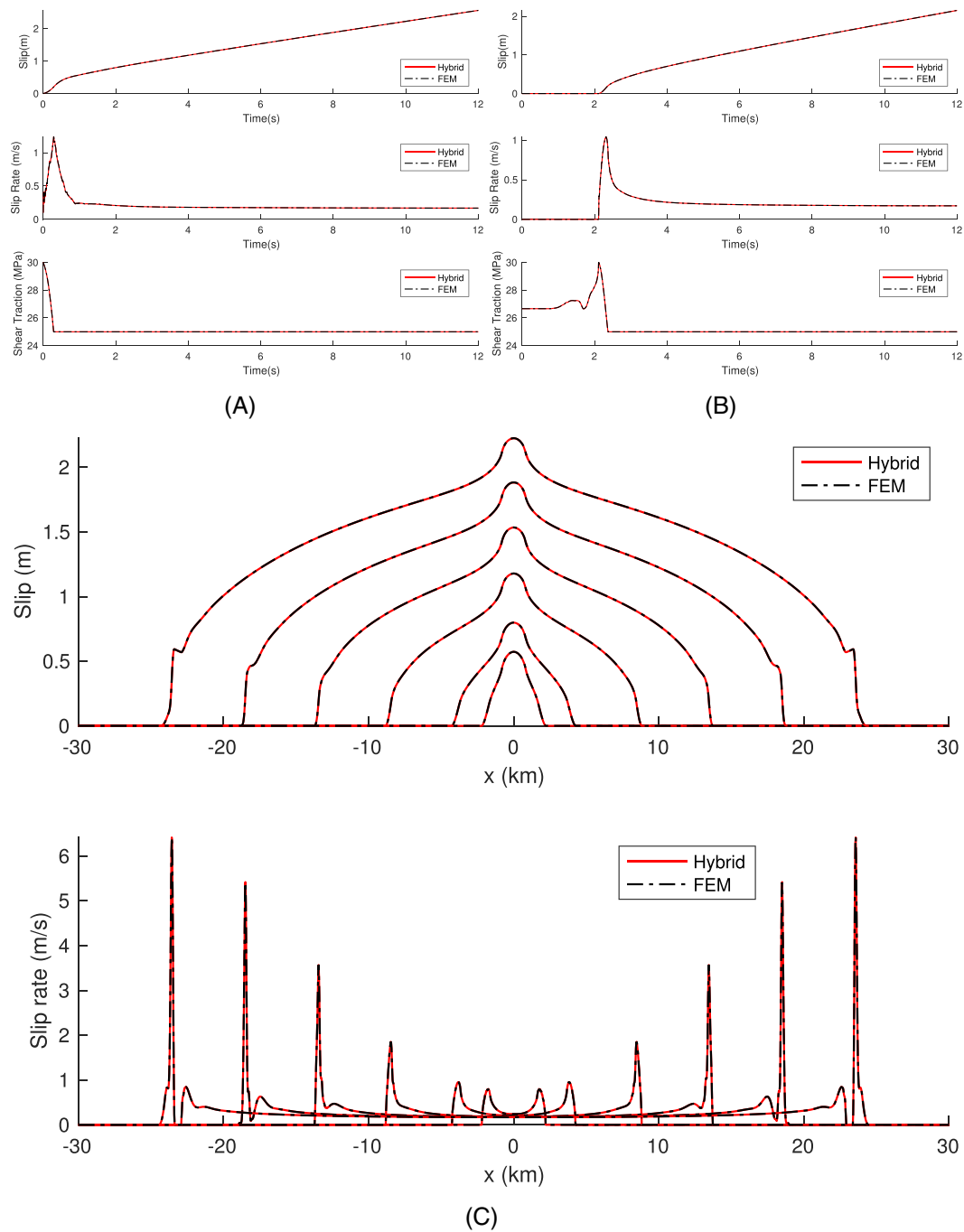


FIGURE 9 Simulation results for a fault embedded in a heterogeneous medium comparing the hybrid method (in red) and the finite element method (FEM; in black) when using a mesh size of $h = 25m$: A, Time history of the slip, slip rate, and shear traction at the station in the center of the fault. B, Time history of the slip, slip rate, and shear traction at the station 4.5 km away from the center of the fault. C, Snapshots of the slip and slip rate at $t = 1s, t = 2s, t = 4s, t = 6s, t = 8s,$ and $t = 10s$. The results from the hybrid method match those from the finite element benchmark solution perfectly in the crack to pulse rupture transition [Colour figure can be viewed at wileyonlinelibrary.com]

In this paper, we implicitly assume that the fault is known a priori. A new fault whose geometry is not a priori known is an important topic to study. One advantage of the proposed hybrid approach is that it can easily adopt volume based discretization techniques with embedded discontinuities such as XFEM^{49,50} or explicit discontinuities such as Discontinuous Galerkin.¹⁹ These methods may replace the continuous Galerkin domain-based method used in this current work. We plan to explore these extensions in the future.

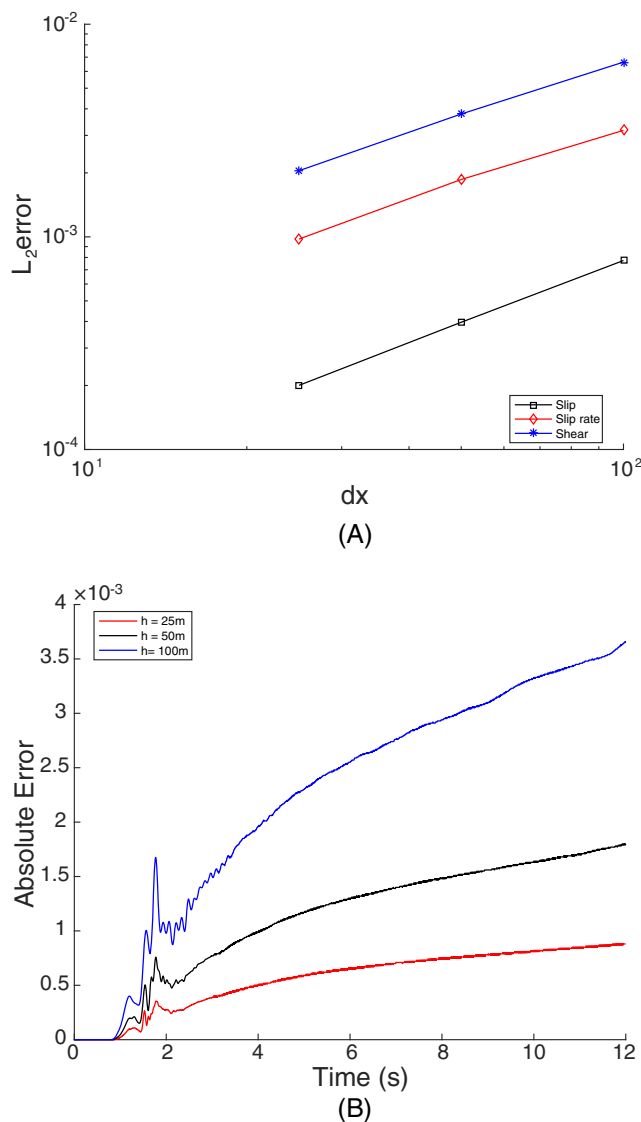


FIGURE 10 Error evolution of hybrid simulation of fault rupture in a LVZ. A, L_2 error for the slip, slip rate, and shear traction versus mesh size. With mesh refinement, the hybrid method converges to the FEM solution. B, The absolute error of the slip rate measured at the center of the fault and its evolution with respect to time for different mesh sizes, $h = 25m$, $h = 50m$, and $h = 100m$. The error is reduced with mesh refinement. The color figure is available in the electronic version only [Colour figure can be viewed at wileyonlinelibrary.com]

Fluids play an important role in the deformation of the fault zone and the surrounding bulk. One advantage of the hybrid method is that it may enable exploring mechanics of fluid infiltrated fault zones with high resolution representation of fault architecture and poromechanical properties distribution within the FEM domain⁵¹ since the saving in the discretization cost would allow using smaller mesh size in the fault zone. Moreover, there exist boundary integral representations for problems of poroelasticity in half space⁵² and viscoelasticity in half space.⁵³ These formulations may be adapted in the hybrid formulation to model poroelastic and viscoelastic deformations in the bulk.

5 | CONCLUSION

We developed a hybrid numerical scheme by integrating the FEM and SBI methods. This hybrid method enables the simulation of wave propagation in unbounded domains with near-source heterogeneities, material nonlinearities, or a complex fault geometry. Specifically, the method is perfectly suited to modeling problems in which heterogeneities or nonlinearities extend over spatial scales that are too large to be lumped into an interfacial traction separation (or friction) law, but yet are much smaller than the overall dimensions of the domain of interest that is affected by wave propagation.

The method is shown to be flexible, accurate, and more efficient than a bulk method such as FEM. The method is primarily useful for earthquake rupture simulations in which the wave source extends primarily in one direction or plane. The main conclusions can be summarized as follows:

1. The hybrid method yields the same results as the pure FEM simulation at a fraction of the discretization cost.
2. The hybrid method significantly reduces the computation cost and memory requirement compared with the FEM because the domain of spatial discretization is truncated.
3. The excellent performance of the hybrid scheme and the absence of artificial reflections from the virtual boundaries suggest that the method may also be used as an accurate near-field wave truncation algorithm.
4. The hybrid method may potentially be used for studying additional small-scale physics within the fault zone and would save memory and other resources that full domain-based discretization numerical schemes would otherwise consume.
5. This method has the potential for use in the field of earthquake cycle simulations in a medium with heterogeneities, nonlinearities, or both because the FEM will capture these features confined in the virtual strip without the need to discretize the entire bulk, whereas the SBI will enable mode truncation and adaptive time stepping to resolve the various scales in time (eg, both rapid slip and interseismic deformations).

ACKNOWLEDGEMENTS

The authors are grateful to Nadia Lapusta, Eric Dunham, J.-P. Ampuero, and Philippe Geubelle for stimulating discussions. This work is supported by the Center for Geologic Storage of CO₂, an Energy Frontier Research Center funded by the U.S. Department of Energy (DOE), Office of Science, Basic Energy Sciences (BES), under Award No. DE-SC0C12504, and by the Southern California Earthquake Center through a collaborative agreement between NSF. Grant Number: EAR0529922 and USGS. Grant Number: 07HQAG0008.

ORCID

Xiao Ma  <http://orcid.org/0000-0002-2125-0880>

REFERENCES

1. Day SM, Dalguer LA, Lapusta N, Liu Y. Comparison of finite difference and boundary integral solutions to three-dimensional spontaneous rupture. *J Geophys Res Solid Earth*. 2005; 110(B12307). <https://doi.org/10.1029/2005JB003813>
2. Chester FM, Chester JS. Ultracataclastic structure and friction processes of the punchbowl fault, San Andreas system, California. *Tectonophysics*. 1998;295(1-2):199-221. <http://www.sciencedirect.com/science/article/pii/S004019519801901218>
3. Erickson BA, Dunham EM, Khosravifar A. A finite difference method for off-fault plasticity throughout the earthquake cycle. *J Mech Phys Solids*. 2016;109:50-77.
4. Lapusta N, Rice JR, Ben-Zion Y, Zheng G. Elastodynamic analysis for slow tectonic loading with spontaneous rupture episodes on faults with rate- and state-dependent friction. *J Geophys Res*. 2000;105:23765.
5. Duan B, Day SM. Inelastic strain distribution and seismic radiation from rupture of a fault kink. *J Geophys Res*. 2008;113(B12):B12311. <http://doi.wiley.com/10.1029/2008JB005847>
6. Ma S, Andrews DJ. Inelastic off-fault response and three-dimensional dynamics of earthquake rupture on a strike-slip fault. *J Geophys Res*. 2010;115(B4):B04304. <http://doi.wiley.com/10.1029/2009JB006382>
7. Dunham EM, Belanger D, Cong L, Kozdon JE. Earthquake ruptures with strongly rate-weakening friction and off-fault plasticity, Part 1: Planar faults. *Bull Seismol Soc Am*. 2011;101(5):2296-2307. <http://www.bssaonline.org/cgi/doi/10.1785/0120100075>
8. Cruz-Atienza VM, Virieux J. Dynamic rupture simulation of non-planar faults with a finite-difference approach. *Geophys J Int*. 2004;158(3):939-954. <https://academic.oup.com/gji/article-lookup/doi/10.1111/j.1365-246X.02291.x>
9. Cruz-Atienza VM, Virieux J, Aochi H. 3D finite-difference dynamic-rupture modeling along nonplanar faults. *GEOPHYSICS*. 2007;72(5):SM123-SM137. <http://library.seg.org/doi/10.1190/1.2766756>
10. Duru K, Dunham EM. Dynamic earthquake rupture simulations on nonplanar faults embedded in 3D geometrically complex, heterogeneous elastic solids. *J Comput Phys*. 2016;305(C):185-207. <http://linkinghub.elsevier.com/retrieve/pii/S0021999115006853>
11. Boore DM, Lerner KL, Aki K. Comparison of two independent methods for the solution of wave-scattering problems: response of a sedimentary basin to vertically incident P waves. *J Geophys Res*. 1971;76(2):558-569. <http://doi.wiley.com/10.1029/JB076i002p00558>
12. Andrews DJ. Rupture propagation with finite stress in antiplane strain. *J Geophys Res*. 1976;81(20):3575.
13. Das S, Aki K. A numerical study of two-dimensional spontaneous rupture propagation. *Geophys J Int*. 1977;50(3):643-668. <http://gji.oxfordjournals.org/cgi/doi/10.1111/j.1365-246X.1977.tb01339.x>

14. Archuleta RJ, Day SM. Dynamic rupture in a layered medium: the 1966 Parkfield earthquake. *Bull Seismol Soc Am.* 1980;70(3):671-689.
15. Day SM. Three-dimensional finite difference simulation of fault dynamics: rectangular faults with fixed rupture velocity. *Bull Seismol Soc Am.* 1982;72(3):705-727.
16. Virieux J, Madariaga R. Dynamic faulting studied by a finite difference method. *Bull Seismol Soc Am.* 1982;72(2):345-369.
17. Kaneko Y, Lapusta N, Ampuero JP. Spectral element modeling of spontaneous earthquake rupture on rate and state faults: effect of velocity-strengthening friction at shallow depths. *J Geophys Res.* 2008;113(B9):B09317. <http://doi.wiley.com/10.1029/2007JB005553>
18. O'Reilly O, Dunham EM, Nordström J. Simulation of wave propagation along fluid-filled cracks using high-order summation-by-parts operators and implicit-explicit time stepping. *SIAM J Sci Comput.* 2017;39(4):B675-B702. <https://doi.org/10.1137/16M1097511>
19. Pelties C, de la Puente J, Ampuero JP, Brietzke GB, Käser M. Three-dimensional dynamic rupture simulation with a high-order discontinuous Galerkin method on unstructured tetrahedral meshes. *J Geophys Res Solid Earth.* 2012;117(B2):B02309. <https://doi.org/10.1029/2011JB008857>
20. Lysmer J, Kuhlemeyer RL. Finite dynamic model for infinite media. *J Eng Mech Div.* 1969;95:859-878.
21. Bettess P. Infinite elements. *Int J Numer Methods Eng.* 1977;11(1):53-64. <http://doi.wiley.com/10.1002/nme.1620110107>
22. Berenger JP. A perfectly matched layer for the absorption of electromagnetic waves. *J Comput Phys.* 1994;114:185-200. <http://www.sciencedirect.com/science/article/pii/S0021999184711594>
23. Hajarolasvadi S, Elbanna AE. A new hybrid numerical scheme for modelling elastodynamics in unbounded media with near-source heterogeneities. *Geophys J Int.* 2017;211(2):851-864. <http://academic.oup.com/gji/article/211/2/851/4082246/A-new-hybrid-numerical-scheme-for-modelling>
24. Ida Y. Cohesive force across the tip of a longitudinal-shear crack and Griffith's specific surface energy. *J Geophys Res.* 1972;77(20):3796-3805. <http://doi.wiley.com/10.1029/JB077i020p03796>
25. Reddy JN. *An Introduction to the Finite Element Method*, Vol. 2. New York: McGraw-Hill; 1993.
26. Hughes TJ. *The Finite Element Method: Linear Static and Dynamic Finite Element Analysis*. MA, US: Courier Corporation; 2012.
27. Courant R, Friedrichs K, Lewy H. Über die partiellen Differenzgleichungen der mathematischen Physik. *Mathematische Annalen.* 1928;100(1):32-74. <https://doi.org/10.1007/BF01448839>
28. Day SM, Dalguer LA, Lapusta N. Comparison of finite difference and boundary integral solutions to three-dimensional spontaneous rupture. *J Geophys Res Solid Earth.* 2005;110:1-23.
29. Geubelle PH, Rice JR. A spectral method for three-dimensional fracture problems. *J Mech Phys Solids.* 1995;43(11):1791-1824.
30. Harris RA, Barall M, Archuleta R, et al. The SCEC/USGS dynamic earthquake rupture code verification exercise. *Seismol Res Lett.* 2009;80(1):119-126. <http://srl.geoscienceworld.org/cgi/doi/10.1785/gssrl.80.1.119>
31. Albertini G, Kammer DS. Off-fault heterogeneities promote supershear transition of dynamic mode II cracks. *J Geophys Res Solid Earth.* 2017;122(8):6625-6641.
32. Ma X, Elbanna AE. Effect of off-fault low-velocity elastic inclusions on supershear rupture dynamics. *Geophys J Int.* 2015;203(1):664-677.
33. Uenishi K, Rice JR. Universal nucleation length for slip-weakening rupture instability under nonuniform fault loading. *J Geophys Res Solid Earth.* 2003;108(B1):2042.
34. Burridge R. Admissible speeds for plane-strain self-similar shear cracks with friction but lacking cohesion. *Geophys J Roy Astron Soc.* 1973;35(4):439-455. <https://doi.org/10.1111/j.1365-246X.1973.tb00608.x>
35. Huang Y, Ampuero JP. Pulse-like ruptures induced by low-velocity fault zones. *J Geophys Res.* 2011;116(December):1-13.
36. Huang Y, Ampuero JP, Helmberger DV. Earthquake ruptures modulated by waves in damaged fault zones. *J Geophys Res Solid Earth.* 2014;119(4):3133-3154. <http://doi.wiley.com/10.1002/2013JB010724>
37. Huang Y, Beroza GC, Ellsworth WL. Stress drop estimates of potentially induced earthquakes in the Guy-Greenbrier sequence. *J Geophys Res Solid Earth.* 2016;121(9):6597-6607. <http://doi.wiley.com/10.1002/2016JB013067>
38. Ma X, Elbanna A. A Model for Athermal Strain Localization in Dry Sheared Fault Gouge. <http://arxiv.org/abs/1701.03087>; 2017.
39. Harari I, Patlashenko I, Givoli D. Dirichlet-to-Neumann maps for unbounded wave guides. *J Comput Phys.* 1998;143(1):200-223. <http://linkinghub.elsevier.com/retrieve/pii/S0021999198959605>
40. Bielak J, MacCamy RC. Symmetric finite element and boundary integral coupling methods for fluid-solid interaction. *Quart Appl Math.* 1991;49(1):107-119.
41. Dieterich JH. Modeling of rock friction: 1. Experimental results and constitutive equations. *J Geophys Res Solid Earth.* 1979;84(B5):2161-2168. <https://doi.org/10.1029/JB084iB05p02161>
42. Ruina A. Slip instability and state variable friction laws. *J Geophys Res Solid Earth.* 1983;88(B12):10359-10370. <http://doi.wiley.com/10.1029/JB088iB12p10359>
43. Bouchbinder E, Langer JS. Nonequilibrium thermodynamics of driven amorphous materials. I. Internal degrees of freedom and volume deformation. *Phys Rev E.* 2009;80(3):31131. <http://link.aps.org/doi/10.1103/PhysRevE.80.031131>
44. Bouchbinder E, Langer JS. Nonequilibrium thermodynamics of driven amorphous materials. II. Effective-temperature theory. *Phys Rev E.* 2009;80(3):31132. <http://link.aps.org/doi/10.1103/PhysRevE.80.031132>
45. Bouchbinder E, Langer JS. Nonequilibrium thermodynamics of driven amorphous materials. III. Shear-transformation-zone plasticity. *Phys Rev E.* 2009;80(3):31133. <http://link.aps.org/doi/10.1103/PhysRevE.80.031133>
46. Poliakov ANB, Dmowska R, Rice JR. Dynamic shear rupture interactions with fault bends and off-axis secondary faulting. *J Geophys Res.* 2002;107(B11):E56—1—E56 6—18. <http://doi.wiley.com/10.1029/2001JB000572>

47. Rice JR, Sammis CG, Parsons R. Off-fault secondary failure induced by a dynamic slip pulse. *Bull Seismol Soc Am.* 2005;95(1):109-134.
48. Templeton EL, Rice JR. Off-fault plasticity and earthquake rupture dynamics: 1. Dry materials or neglect of fluid pressure changes. *J Geophys Res Solid Earth.* 2008;113(9):1-19.
49. Liu F, Borja RI. An extended finite element framework for slow-rate frictional faulting with bulk plasticity and variable friction. *Int J Numer Anal Methods Geomech*; 33(13):1535-1560. <https://onlinelibrary.wiley.com/doi/abs/10.1002/nag.777>
50. Liu F, Borja RI. Extended finite element framework for fault rupture dynamics including bulk plasticity. *Int J Numer Anal Methods Geomech*; 37(18):3087-3111. <https://onlinelibrary.wiley.com/doi/abs/10.1002/nag.2179>
51. White JA, Borja RI. Stabilized low-order finite elements for coupled solid-deformation/fluid-diffusion and their application to fault zone transients. *Comput Methods Appl Mech Eng.* 2008;197(49):4353-4366. <http://www.sciencedirect.com/science/article/pii/S004578250801ignorespaces02016>
52. Chen YS, Lo WC, Leu JM, Cheng AHD. Effect of impermeable boundaries on the propagation of rayleigh waves in an unsaturated poroelastic half-space. *J Mech.* 2010;26(4):501-511.
53. Danyluk MJ, Geubelle PH, Hilton HH. Two-dimensional dynamic and three-dimensional fracture in viscoelastic materials. *Int J Solids Struct.* 1998;35(28):3831-3853. <http://www.sciencedirect.com/science/article/pii/S002076839701ignorespaces02217>
54. Breitenfeld MS, Geubelle PH. Numerical analysis of dynamic debonding under 2D in-plane and 3D loading. *Int J Fract.* 1998;93(1-4):13-38.

How to cite this article: Ma X, Hajarolasvadi S, Albertini G, Kammer D, Elbanna A. A hybrid finite element-spectral boundary integral approach: Applications to dynamic rupture modeling in unbounded domains. *Int J Numer Anal Methods Geomech.* 2018;1-22. <https://doi.org/10.1002/nag.2865>

APPENDIX A: TRACTION-AT-SPLIT-NODE METHOD

The traction-at-split node (TSN) method presented here is adopted from Day et al²⁸ with modifications for the 2D in-plane problem.

As shown in Figure A1, a given fault plane node is split into plus- and minus-side parts. The interaction between the two half-split nodes is only through the traction acting on the interface between them. The plus- and minus-side nodes have respective masses of M^+ and M^- and experience the elastic restoring forces f^+ and f^- . At time $t + \Delta t/2$, D'Alembert's principle leads to a force balance, including the inertial force for each split node. When the central difference scheme is used in time, the velocity $\dot{u}_v^\pm(t + \Delta t/2)$ and displacement $u_v^\pm(t + \Delta t)$ components at the arbitrary split nodes (i, j) are the following:

$$\dot{u}_v^\pm(t + \Delta t/2) = \dot{u}_v^\pm(t - \Delta t/2) + \Delta t(M^\pm)^{-1} \cdot \{f_v^\mp(t) \mp aT_v(t) \pm aT_v^0\}, \quad (\text{A1})$$

$$u_v^\pm(t + \Delta t) = u_v(t) + \Delta t \dot{u}_v^\pm(t + \Delta t/2) \quad v = x_1, x_2, \quad (\text{A2})$$

where a is the area of the fault surface associated with the split node at (j, k), Δt is the time step, T_v is the fault plane traction vector at node (j, k), and T_v^0 is the initial equilibrium value of T_v .

By enforcing the continuity of the tangential velocity ($\dot{u}_1^+ - \dot{u}_1^- = 0$) and the continuity of normal displacement ($u_2^+ - u_2^- = 0$) and plugging Equation A1 and Equation A2 into the two continuity equations, we were able to derive the sticking traction \tilde{T}_1 and \tilde{T}_2 as follows:

$$\tilde{T}_1 = \frac{\Delta t^{-1} M^+ M^- (\dot{u}_1^+ - \dot{u}_1^-) + M^- f_1^+ - M^+ f_1^-}{a(M^+ + M^-)} + T_1^0, \quad (\text{A3})$$

$$\tilde{T}_2 = \frac{\Delta t^{-1} M^+ M^- [(u_2^+ - u_2^-) + \Delta t^{-1} (u_2^+ - u_2^-)] + M^- f_2^+ - M^+ f_2^-}{a(M^+ + M^-)} + T_2^0. \quad (\text{A4})$$

The jumping condition of the fault will be satisfied if the fault traction T_v is as follows:

$$T_v = \begin{cases} \tilde{T}_1, & v = x_1, & \tilde{T}_1 \leq \tau_f \\ \tau_c, & v = x_1, & \tilde{T}_1 > \tau_f \\ \tilde{T}_2, & v = x_2, & \tilde{T}_2 \leq 0 \\ 0, & v = x_2, & \tilde{T}_2 > 0. \end{cases} \quad (\text{A5})$$

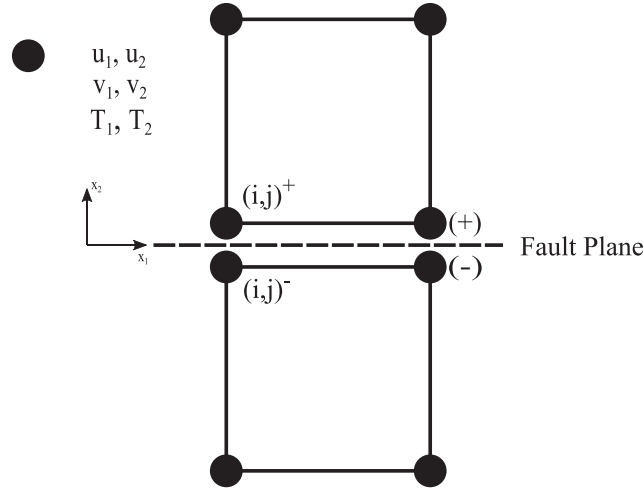


FIGURE A1 Illustration of the traction-at-split-node method. The node (i,j) indicates the nodes on the fault. The displacements u_1, u_2 are the displacements in two directions at the fault nodes, the velocities v_1, v_2 are the velocities in two directions at the fault nodes, and the stresses T_1, T_2 are the stresses in two directions at the fault nodes

The formulation above enforces the jump and parallel conditions for the fault. It also governs the fault behavior at all times, such as at nucleation, arrest of rupture, and subsequent reactivation and arrest of rupture.

APPENDIX B: INDEPENDENT SPECTRAL FORMULATION

The material in this section is extensively borrowed from Geubelle and Rice,²⁹ in which a more general treatment of the problem is provided.

$$u_1(x_1, x_2, t) = \phi_{,1}(x_1, x_2, t) + \psi_{,2}(x_1, x_2, t), \quad (\text{B1})$$

$$u_2(x_1, x_2, t) = \phi_{,2}(x_1, x_2, t) - \psi_{,1}(x_1, x_2, t), \quad (\text{B2})$$

where

$$c_p^2 \Delta \phi = \frac{\partial^2 \phi}{\partial t^2}, \quad c_s^2 \Delta \psi = \frac{\partial^2 \psi}{\partial t^2}.$$

We examine one particular spectral component:

$$[\phi(x_1, x_2, t), \psi(x_1, x_2, t)] = e^{iqx_1} [\Phi(x_2, t; q), \Psi(x_2, t; q)]. \quad (\text{B3})$$

The Laplace transform of a function f is introduced as follows:

$$\hat{f}(p) = L[f(t)] = \int_0^\infty e^{-pt} f(t) dt.$$

Therefore,

$$\begin{aligned} \frac{\partial^2 \hat{\Phi}}{\partial x_2^2}(x_2, p; q) &= q^2 \alpha_p^2 \hat{\Phi}(x_2, p; q) \\ \frac{\partial^2 \hat{\Psi}}{\partial x_2^2}(x_2, p; q) &= q^2 \alpha_s^2 \hat{\Psi}(x_2, p; q), \end{aligned} \quad (\text{B4})$$

where

$$\alpha_p = \sqrt{1 + \frac{p^2}{q^2 c_p^2}}, \quad \alpha_s = \sqrt{1 + \frac{p^2}{q^2 c_s^2}}.$$

For $x_2 > 0$,

$$\hat{\Phi}(x_2, p; q) = \hat{\Phi}_0(p; q) e^{-|q| \alpha_p x_2}, \quad (\text{B5})$$

$$\hat{\Psi}(x_2, p; q) = \hat{\Psi}_0(p; q) e^{-|q| \alpha_s x_2}. \quad (\text{B6})$$

Substituting Equation B5 and Equation B6 in Equation B1 and Equation B2 gives

$$\begin{aligned}\hat{U}_1(x_1, x_2, t) &= e^{iqx_1} \left(iq\hat{\Phi}_0(p; q)e^{-|q|\alpha_p x_2} - |q|\alpha_s \hat{\Psi}_0(p; q)e^{-|q|\alpha_s x_2} \right) \\ \hat{U}_2(x_1, x_2, t) &= e^{iqx_1} \left(-|q|\alpha_p \hat{\Phi}_0(p; q)e^{-|q|\alpha_p x_2} - iq\hat{\Psi}_0(p; q)e^{-|q|\alpha_s x_2} \right).\end{aligned}\quad (\text{B7})$$

We are primarily concerned with tractions along $x_2 = 0$. Therefore,

$$u_j(x_1, x_2 = 0^+, t) = U_j(t; q)e^{iqx_1}. \quad (\text{B8})$$

Thus,

$$\hat{U}_1(p; q) = iq\hat{\Phi}_0(p; q) - |q|\alpha_s \hat{\Psi}_0(p; q), \quad (\text{B9})$$

$$\hat{U}_2(p; q) = -|q|\alpha_p \hat{\Phi}_0(p; q) - iq\hat{\Psi}_0(p; q). \quad (\text{B10})$$

Solving for $\hat{\Phi}_0(p; q)$ and $\hat{\Psi}_0(p; q)$ yields

$$\hat{\Phi}_0(p; q) = \frac{-iq\hat{U}_1(p; q) + |q|\alpha_s \hat{U}_2(p; q)}{q^2(1 - \alpha_s \alpha_p)}, \quad \hat{\Psi}_0(p; q) = \frac{|q|\alpha_p \hat{U}_1(p; q) + iq\hat{U}_2(p; q)}{q^2(1 - \alpha_s \alpha_p)}, \quad (\text{B11})$$

$$\begin{aligned}\hat{U}_1 &= e^{i|q|x_1} \left\{ \hat{U}_1(p; q) \frac{e^{-|q|\alpha_p x_2} - \alpha_s \alpha_p e^{-|q|\alpha_s x_2}}{1 - \alpha_s \alpha_p} \right. \\ &\quad \left. + \hat{U}_2(p; q) \frac{iq\alpha_s}{|q|(1 - \alpha_s \alpha_p)} (e^{-|q|\alpha_p x_2} - e^{-|q|\alpha_s x_2}) \right\},\end{aligned}\quad (\text{B12})$$

$$\begin{aligned}\hat{U}_2 &= e^{i|q|x_1} \left\{ \hat{U}_1(p; q) \frac{iq\alpha_p}{|q|(1 - \alpha_s \alpha_p)} (e^{-|q|\alpha_p x_2} - e^{-|q|\alpha_s x_2}) \right. \\ &\quad \left. + \hat{U}_2(p; q) \frac{e^{-|q|\alpha_s x_2} - \alpha_s \alpha_p e^{-|q|\alpha_p x_2}}{1 - \alpha_s \alpha_p} \right\}.\end{aligned}\quad (\text{B13})$$

Using the stress-strain relation $\sigma_{ij} = \lambda \delta_{ij} u_{k,k} + \mu(u_{i,j} + u_{j,i})$ and writing the shear stress components along the fault as $\tau_j(x_1, t) = \sigma_{2j}(x_1, x_2 = 0^+, t) = T_j(t; q)e^{iqx_1}$ yields

$$\hat{T}_1(p; q) = -\mu|q| \frac{\alpha_p(1 - \alpha_s^2)}{1 - \alpha_s \alpha_p} \hat{U}_1(p; q) + i\mu q \left(2 - \frac{1 - \alpha_s^2}{1 - \alpha_s \alpha_p} \right) \hat{U}_2(p; q), \quad (\text{B14})$$

$$\hat{T}_2(p; q) = -i\mu q \left(2 - \frac{1 - \alpha_s^2}{1 - \alpha_s \alpha_p} \right) \hat{U}_1(p; q) - \mu|q| \frac{\alpha_s(1 - \alpha_s^2)}{1 - \alpha_s \alpha_p} \hat{U}_2(p; q). \quad (\text{B15})$$

Decoupling the equations and extracting the instantaneous response gives the following:

$$\hat{T}_1(p; q) = -\frac{\mu}{c_s} p \hat{U}_1(p; q) - \mu \left\{ |q| \frac{4\alpha_s \alpha_p - (1 + \alpha_s^2)}{\alpha_s(1 - \alpha_s^2)} - \frac{p}{c_s} \right\} \hat{U}_1(p; q), \quad (\text{B16})$$

$$\hat{T}_2(p; q) = -\frac{(\lambda + 2\mu)}{c_p} p \hat{U}_1(p; q) - \left\{ |q|\mu \frac{4\alpha_s \alpha_p - (1 + \alpha_s^2)}{\alpha_p(1 - \alpha_s^2)} - \frac{\lambda + 2\mu}{c_s} p \right\} \hat{U}_2(p; q), \quad (\text{B17})$$

for the upper half-plane. Similar expressions can be obtained for the lower half-plane. In the time domain, these relationships translate to the following:

$$\begin{aligned}\tau_1^\pm(x_1, t) &= \tau_0(x_1, t) \mp \frac{\mu}{c_s} \frac{\partial u_1^\pm}{\partial t} + f_1^\pm(x_1, t), \\ \tau_2^\pm(x_1, t) &= \tau_0(x_1, t) \mp \frac{(\lambda + 2\mu)}{c_p} \frac{\partial u_2^\pm}{\partial t} + f_2^\pm(x_1, t),\end{aligned}\tag{B18}$$

where f is a linear functional of the prior deformation history and can be expressed in terms of its spectral components as $f_j(x_1, t) = F_j(t; q)e^{iqx_1}$. These components are given in Breitenfeld and Geubelle⁵⁴ as follows:

$$\begin{aligned}F_1^\pm(t; q) &= \mp \mu |q| \int_0^t H_{11}(|q|c_s t') U_1^\pm(t - t'; q) |q| c_s dt' + i(2 - \eta) \mu q U_2^\pm(t; q) \\ &\quad + i \mu q \int_0^t H_{12}(|q|c_s t') U_2^\pm(t - t'; q) |q| c_s dt', \\ F_2^\pm(t; q) &= \mp \mu |q| \int_0^t H_{22}(|q|c_s t') U_2^\pm(t - t'; q) |q| c_s dt' - i(2 - \eta) \mu q U_1^\pm(t; q) \\ &\quad - i \mu q \int_0^t H_{12}(|q|c_s t') U_1^\pm(t - t'; q) |q| c_s dt',\end{aligned}\tag{B19}$$

where $\eta = c_p/c_s$ and H_{ij} are the convolution kernels, which are defined by the following inverse Laplace transforms:

$$\begin{aligned}H_{11}(T) &= L^{-1} \left[\frac{s^2 \sqrt{s^2 + \eta^2}}{\sqrt{s^2 + \eta^2} \sqrt{s^2 + 1} - \eta} - s \right], \\ H_{12}(T) &= L^{-1} \left[\frac{\eta s^2}{\eta - \sqrt{s^2 + \eta^2} \sqrt{s^2 + 1}} + \eta \right], \\ H_{22}(T) &= L^{-1} \left[\frac{s^2 \sqrt{s^2 + 1}}{\sqrt{1 + s^2/\eta^2} \sqrt{s^2 + 1} - 1} - \eta s \right],\end{aligned}\tag{B20}$$

where $s = p/|q|c_s$ is the nondimensional Laplace transform variable. The kernels can be inverted numerically.